Design and analysis of a SF6 Gas Insulating HV-Bushing for CRAFT NNBI*

Yu-Chen Qu,[1,2] Zhi-Min Liu,[1,2,†] Cai-Chao Jiang,[1,2] Jiang-Long Wei,[1] Bo Liu,[1,2] Yuan-Lai Xie,[1,2] and Xu Wang[3]

[1] *Institute of Plasma Physics, Hefei Institutes of Physical Science, Chinese Academy of Sciences, Hefei 230031, China*
[2] *University of Science and Technology of China, Hefei 230026, China*
[3] *China Nuclear Engineering Consulting Co., Ltd., Beijing 100032, China*

The full-scale beam source of CRAFT NNBI is planned to adopt a vacuum-insulated ion source scheme to generate a $400\,\mathrm{keV}$ negative hydrogen ion beam through two stages of $-200\,\mathrm{kV}$ acceleration voltage. A preliminary design has been developed for two stages of $-400\,\mathrm{kV}$ high-voltage bushings, which are intended for insulating and sealing connections between the SF6-insulated transmission line and the vacuum chamber. Vacuum-side insulation design has been conducted to analyze and improve the electric field strength of the vacuum-side cathode surface, anode surface, insulator surface, and triple point, meeting the standard requirements specified by the Japan Atomic Energy Agency for high-voltage bushings designed for ITER. The design includes the cooling water flow channels for the $-200\,\mathrm{kV}$ bushing section, considering the requirements for cooling water flow rate based on the thermal load of the accelerating electrode (AG) and temperature constraints, analyzing pressure drop in the channels and uniformity of flow distribution. Mechanical strength analysis of the bushing structure has been performed, considering the stress and deformation under $0.6\,\mathrm{MPa}$ SF6 gas, $1\,\mathrm{MPa}$ air, and gravity loads between the insulating ceramic ring and fiber-reinforced plastic (FRP) ring within the transmission line.

Keywords: NNBI, HV bushing, Vacuum insulation, Cooling water channel, Structural strength

I. INTRODUCTION

The Comprehensive Research Facility for Fusion Reactor Key Technology (CRAFT) is a major scientific infrastructure project under China's "13th Five-Year Plan" for major scientific infrastructure construction. The goal of CRAFT is to establish an internationally leading comprehensive research and testing platform in the field of nuclear fusion, with the highest parameters and most complete functions. One of the components is the Neutral Beam Injection system within the Negative ion source (NNBI) of CRAFT, which is preliminarily planned to achieve a hydrogen neutral beam with an energy of $200\,\mathrm{keV}$-$400\,\mathrm{keV}$, power of $2\,\mathrm{MW}$, and pulse width greater than $100\,\mathrm{s}$ [1].

The neutral beam ion source adopts an electrostatic field acceleration method, and high-energy beam currents require high-voltage acceleration, thereby posing various challenges related to high-voltage insulation. Research by Hodgson *et al.* on the insulation gas of the ITER NBI system has shown that radiation-induced leakage currents in air and SF6 gas can lead to unacceptable high power losses [2], prompting the proposal of a vacuum-insulated NBI ion source scheme. The ion source is placed in a vacuum chamber, and the required electrical energy, cooling water, and gas supply enter the vacuum chamber through HV bushings from the external SF6 gas-insulated transmission line. In order to verify the performance required by the ITER NBI, the ITER NBI test facility NBTF [3] was constructed in Padua, Italy. JAEA has conducted long-term research on high-voltage insulation aspects of NBI [4] and manufactured high-voltage components for the $1\,\mathrm{MV}$ DC power supply system of NBTF and ITER NBI. This includes a $200\,\mathrm{kV}$ first-stage 5-pole $1\,\mathrm{MV}$ HV bushing design, which has passed withstand tests [5], providing relevant design guidelines for reference.

CRAFT NNBI plans to develop a vacuum insulation scheme and has already initiated research and development work on the negative ion source and SF6 transmission line [6, 7], with the beam source test facility under construction. This paper presents preliminary design work on HV bushings, including: 1. Vacuum insulation design, analysis of the electric field at the vacuum-side electrode, insulator, and cathode triple point. 2. High-speed cooling water flow channel design, analysis of cooling water flow pressure drop and flow distribution in multiple parallel channels. 3. Mechanical structure design, considering insulation gas pressure and gravity loads, and analyzing structural stress and mechanical deformation.

II. OVERALL DESIGN OF HV BUSHINGS

The structure of the HV bushings is shown in Fig. 1, consisting of two levels of bushings at $-400\,\mathrm{kV}$ and $-200\,\mathrm{kV}$ coaxially nested together. The bushings' electrostatic screens are fixed to the flanges, with ceramic rings and fiber-reinforced plastic rings (FRP) coaxially positioned between the flanges to provide insulation, support, and sealing. The inner side of the bushings is under vacuum, while the outer side is connected to the SF6 transmission line, filled with SF6 insulation gas at a pressure of $0.6\,\mathrm{MPa}$. Dry air at a pressure greater than $0.6\,\mathrm{MPa}$ is present between the ceramic rings and fiber-reinforced plastic rings to prevent SF6 gas leakage into the vacuum. The ceramic rings are brazed sealed to Kovar rings, while the fiber-reinforced plastic rings and Kovar rings are sealed to the bushings flanges using sealing rings in a compression manner. The structure simplification ignores the structure of the SF6 transmission line section and the cooling

* Supported by the National Natural Science Foundation of China (11975263), (11975264); National Major Science and Technology Infrastructure Project of China(2018-000052-73-01-001228)

† Corresponding author, liu@ipp.ac.cn

water flow channel section of the $-200\,\mathrm{kV}$ bushings.

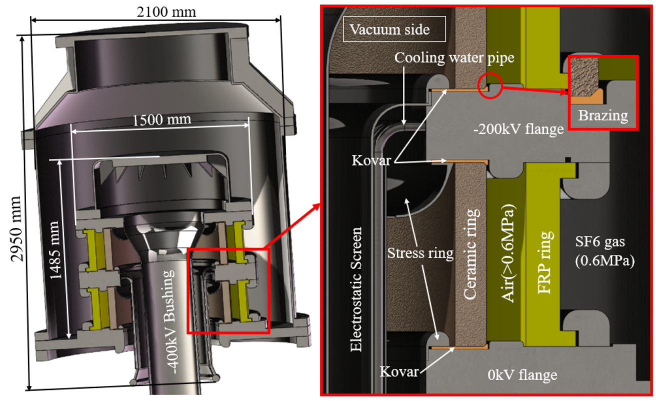

Fig. 1. Cross sectional view of CRAFT NNBI HV bushing.

The CRAFT NNBI ion source has been designed in previous work, Fig. 2 shows the power supply structure and estimated power load of the accelerator section [7]. The accelerator is divided into four layers. The ground grid (GG) is at the same potential as the vacuum chamber wall. The acceleration grid (AG) is connected to the $-200\,\mathrm{kV}$ bushings for power supply. The inner diameter of the $-200\,\mathrm{kV}$ electrostatic screen is $295\,\mathrm{mm}$, and the outer diameter is $325\,\mathrm{mm}$. The bottom of the electrostatic screen expands and is equipped with a pressure equalization ring to reduce the electric field intensity. The outer diameter of the pressure equalization ring is smaller than the inner diameter of the $0\,\mathrm{kV}$ flange for ease of engineering assembly. Due to space limitations, compact high-speed cooling water flow channels need to be designed to dissipate the $500\,\mathrm{kW}$ heat load from the AG, as shown in Fig. 3. The six parallel pipelines on the electrostatic screen form a set of flow channels, intersecting inside the flange and at the bottom of the pressure equalization ring. There are a total of four sets of cooling water flow channels, with two sets each flowing in and out of the AG. Additional shielding housings are installed on the external of the pipelines on the electrostatic screen to shield the electric field and prevent field concentration near the pipelines, reducing insulation performance. The extraction grid (EG) is connected to the $-400\,\mathrm{kV}$ bushings for power supply. The power supply for the plasma grid (PG), RF plasma source, EG cooling water pipelines, etc., are all located inside the outer diameter of the $-400\,\mathrm{kV}$ bushings, which is $430\,\mathrm{mm}$. The lower end of the electrostatic screen is directly connected to the plasma source of the accelerator, thus eliminating the need for a pressure equalization ring.

III. VACUUM INSULATION

A. Design standards

The HV bushing has two insulation clearances to maintain a $400\,\mathrm{kV}$ voltage. H. Tobari. *et al* experimentally studied the voltage maintenance capability of HV bushings with multiple clearances and provided an empirical formula for voltage maintenance capability [8],

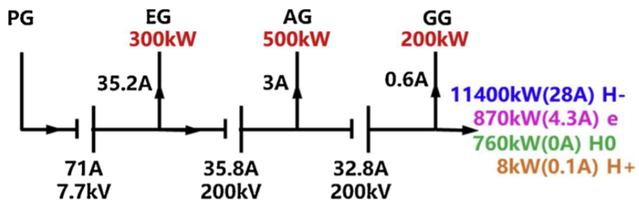

Fig. 2. Accelerator power supply and power estimation.

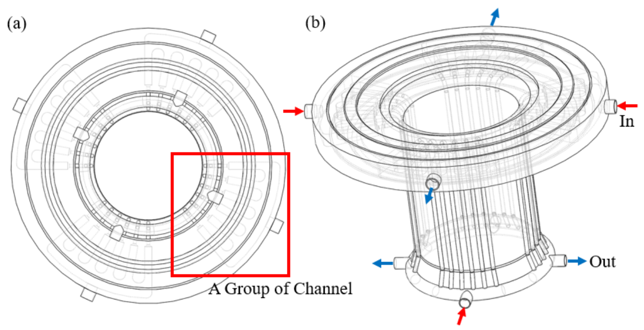

Fig. 3. $-200\,\mathrm{kV}$ screen cooling water channel. bottom view (a), oblique view(b).

$$(EV)^{0.5} = \frac{V}{(r_c ln(r_a/r_c))^{0.5}} > k^{0.5} = 36S6{-}0.18 \quad (1)$$

Where $E(kV/mm)$ is the electric field strength on the cathode surface and $V(kV)$ is the gap maintenance voltage. Considering the HV bushing as a coaxial electrode, the electric field on the cathode surface is calculated by the outer electrode radius, r_a, and the inner electrode radius, r_c. According to the Clump theory [9], breakdown occurs when the product of the charge Q and the voltage V exceeds a certain threshold. Since Q is proportional to the electric field strength on the electrode surface, the product of Q and V is converted into the product of E and V, with a corresponding threshold value, k, related to the sum of the cathode total area, $S(m^2)$.

Antonio Masiello proposed some key design standards for electric field limitations in HV bushing vacuum insulation [10] and compared them with another design standard [11], as shown in Tab. 1 The Japan Atomic Energy Agency (JAEA) designed the ITER NNBI HV bushing with reference to this standard [12], but the electric field at the cathode triple point did not meet the standard limits. JAEA conducted high-voltage maintenance tests for verification [5], demonstrating that the limitations provided by this design standard are reliable. However, for the HV bushings designed for NBTF, a cathode surface electric field limit standard of 3 kV/mm was adopted with a margin consideration [13]. It is important to note that the surface electric field amplitude refers to the region near the surface, not directly on the surface. The strictly defined on-surface electric field amplitude is the average of the electric field amplitudes near both sides

of the surface. The surface electric field mentioned in this paper refers to the electric field in the region near the surface.

B. Bushing design

The main design parameters of the CRAFT NNBI HV bushing are shown in Tab. 2 The values for electric field limitations were comprehensively determined based on relevant experimental results and design standards. Considering the dimensions of internal pipes and cables, the diameter of the $-400\,\mathrm{kV}$ electrostatic shield was first determined, followed by calculating the dimensions of other electrostatic shields based on the electric field limitations. The voltage maintenance capability for each gap was calculated using empirical Eq. 1. The cathode area for the $-400\,\mathrm{kV}$ to $-200\,\mathrm{kV}$ gap is $1.89\,\mathrm{m}^2$, with a voltage maintenance capability of $238\,\mathrm{kV}$. For the $-200\,\mathrm{kV}$ to $0\,\mathrm{kV}$ gap, the cathode area is $1.52\,\mathrm{m}^2$, with a voltage maintenance capability of $263\,\mathrm{kV}$, meeting the design requirements. While ensuring insulation capability, it is desired to minimize the overall size of the bushing as much as possible. This can reduce costs, especially since larger ceramic insulating rings are more expensive, and the brazing technology for ceramic rings and Kovar rings is limited by size. Additionally, smaller size implies greater structural strength and vacuum maintenance reliability. Based on the dimensions of the main components, a COMSOL software analysis was conducted to adjust the geometric shape of a 2D axisymmetric model for electric field analysis, resulting in a structural model with electric field amplitudes that meet design standards, as shown in Fig. 4 The maximum electric field value on the cathode surface of the electrostatic shield is approximately $2.9\,\mathrm{kV/mm}$. The electric field on the anode surface increases at stress rings and other bending points, but the electric field amplitudes at all locations are below the limit. The function of the stress ring (shown in Fig. 1) is similar to a pressure ring, but its main purpose is to reduce the electric field amplitude at the triple point. According to the standard in Tab. 1, the electric field amplitude at the cathode triple point should be less than $0.1\,\mathrm{kV/mm}$ to prevent surface flashover. This is a very stringent limitation, so an asymmetric stress ring design was implemented, with a larger cathode stress ring and a smaller anode stress ring, while both gaps have the same stress ring size. However, the electric field amplitude at the cathode triple point does not meet the design standard.

Increasing the size of the stress ring further does not effectively reduce the electric field amplitude at the triple point. Increasing the diameter of the stress ring to bring it closer to the ceramic insulating ring can lower the electric field amplitude, but the distance between them cannot be too close, considering manufacturing precision, and is set $2\,\mathrm{mm}$. Additionally, adding a raised metal ring on the flange between the ceramic ring and the FRP ring can reduce the electric field amplitude at the triple point, but it also increases the electric field amplitude on the surface of the ceramic insulating ring facing the vacuum side. Ultimately, it was decided to have a

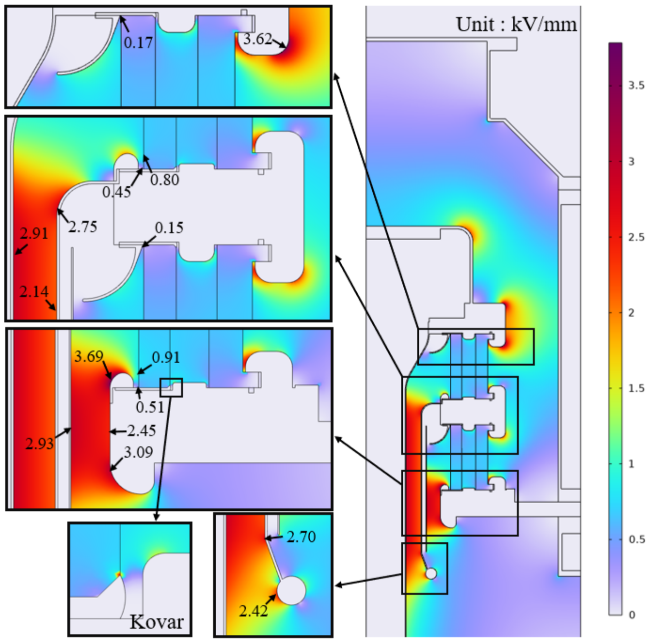

Fig. 4. Electric field amplitude for a 2D analysis.

$3\,\mathrm{cm}$ high metal ring on the cathode and a $1\,\mathrm{cm}$ high metal ring on the anode. The electric field amplitude at the cathode triple point for the $-400\,\mathrm{kV}$ flange is $0.17\,\mathrm{kV/mm}$, and for the $-200\,\mathrm{kV}$ flange is $0.15\,\mathrm{kV/mm}$, which does not meet the design standard but satisfies the DDD 5.3 standard.

The cathode triple point electric field in the HV bushing design for ITER NNBI did not meet the design standard, but its reliability was verified through high-voltage maintenance tests. The cathode triple point electric field amplitude in the CRAFT NNBI bushing design is lower than that of ITER NNBI. During the brazing of ceramic and Kovar rings, there may be overflow of brazing material forming irregular boundaries. Therefore, the design includes embedding the Kovar ring into the flange to a certain depth, with the brazing area shielded by the metal ring on the flange to have a very low electric field amplitude, avoiding irregular boundaries of brazing material enhancing the electric field beyond design limits.

The analysis of the 2D axisymmetric electric field cannot calculate the electric field near the cooling water pipes on the $-200\,\mathrm{kV}$ electrostatic screen. In order to ensure the reliability of the insulation design, a 3D electric field analysis of the $-200\,\mathrm{kV}$ electrostatic screen was conducted, and the results are shown in Fig. 5. The electric field near the cooling water pipes is non-uniform, with the maximum electric field magnitude appearing at the edge of each group of cooling water pipes being $1.37\,\mathrm{kV/mm}$. Non-uniform electric fields also appear at the edges of the shielding shell of the pipes, and the distribution pattern is influenced by the arrangement of the pipes. The electric field magnitude obtained from the three-dimensional analysis is slightly smaller than that from the two-dimensional analysis, and finite element analysis is limited by the grid size, which may cause distortion of the

TABLE 1. Design criteria for vacuum electric field in the HV bushing.

Position	Electric field limits (kV/mm)	DDD5.3 limit (kV/mm)
Cathode surface (200 kV)	< 4	< 10
Cathode surface (1000 kV)	< 3	—
Insulator surface	< 1	—
Cathode triple point	< 0.1	< 1

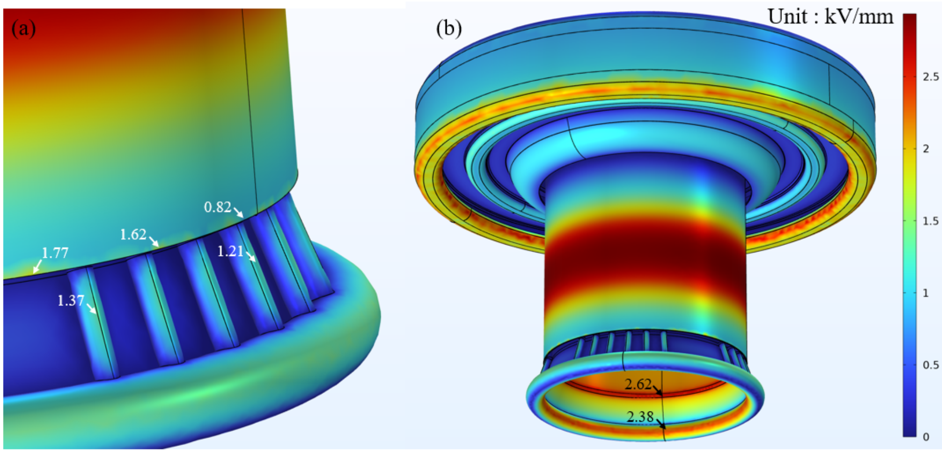

Fig. 5. -200 kV electrostatic screen electric field amplitude for a 3D analysis. around cooling water pipes (a), screen overall (b).

TABLE 2. Main design parameters of CRAFT NNBI HV bushing.

Parameter	Value
Cathode surface electric field	< 3 kV/mm
Other electrode surface electric field	< 4 kV/mm
Insulator surface	< 1 kV/mm
Cathode triple point	< 0.17 kV/mm
-400 kV screen diameter	430 mm
-400 kV ~ -200 kV gap length	80 mm
-200 kV screen diameter	650 mm
-200 kV ~ 0 kV gap length	75 mm
Flange diameter	1500 mm
Ceramic ring diameter	1030 mm
FRP ring diameter	1310 mm

electric field in small structures. However, the electric field magnitudes in all areas are far below the standard limits.

IV. COOLING WATER CHANNEL

When the CRAFT NNBI ion source operates at full power, it is expected to generate a heat load of 500 kW on the AG due to the bombardment of charged particles. In order to meet the requirements of long-pulse operation, an equally powerful cooling capacity is needed, thus a high-speed cooling water flow channel is designed. Under normal operating conditions, the cooling water temperature can rise to over 30 °C during steady-state operation of the accelerator, corresponding to a mass flow rate of approximately 4 kg/s. However, for the design of the accelerator, it is desired to minimize the deformation of the electrodes caused by temperature changes in order to achieve more stable accelerator performance. According to calculations based on a 6 °C temperature rise of the cooling water, the mass flow rate of the cooling water is approximately 20 kg/s. The four sets of channels are divided into two inlet and two outlet groups, with each group of channels carrying half of the total flow rate. Using the Fluent software k-ω model, the flow analysis in the AG direction for a set of channels with mass flow rates ranging from 2 to 10 kg/s for both inflow and outflow was conducted.

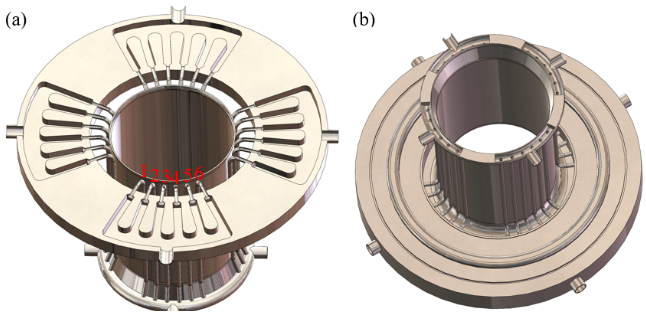

Fig. 6. Cross sectional view of cooling water channel. Inside the flange (a), Inside the grading ring (b).

The cross-sectional views of the cooling water flow channels in the electrostatic screen and flange are shown in Fig. 6, illustrating the internal structures of the upper flange and the bottom equal pressure ring of the flow channels. The cross-sectional area of the above two parts of the channels is much larger than that of the six parallel pipes, concentrating the pressure gradient at the entrance of the pipes, which can suppress flow instability in the parallel channels and help balance

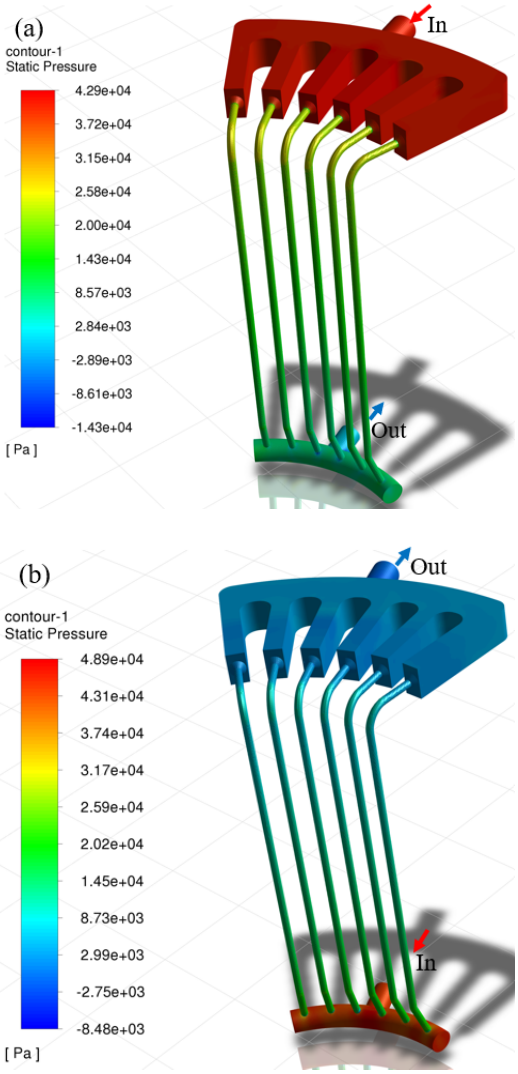

Fig. 7. The pressure distribution in the channel with a 6 kg/s mass flow rate. Cooling water flows into the AG direction (a), Cooling water flows out of AG direction (b).

the flow distribution. Fig. 7 shows the pressure distribution inside the channels when the mass flow rate is $6\,\mathrm{kg/s}$, with significant pressure drops at the entrances of the six parallel pipes for both inflow and outflow, accounting for approximately 50% and 60% of the total pressure drop, respectively, without flow instability between the parallel pipes observed in the simulation. The pressure drop variations in the channels are shown in Fig. 8, with the pressure drop in the inflow direction of the AG being lower than that in the outflow direction. At maximum flow rate, the inlet pressure drop is $109.9\,\mathrm{kPa}$, while the outlet pressure drop is $117.1\,\mathrm{kPa}$, a difference of 6.5%. The flow distribution within the parallel pipes is shown in Fig. 9, with better uniformity in the inflow direction of the AG compared to the outflow direction. At a mass flow rate of $8\,\mathrm{kg/s}$, the deviation in flow distribution is greatest, with forward flow deviation at 8.3% and reverse flow deviation at 11.5%. Since the inlet and outlet of the channels are positioned at the center of pipes 3 and 4, these two pipes have higher flow rates in all cases, and the distribution uniformity does not follow a consistent pattern with flow rate. The performance of the inflow direction of the AG is better than that of the outflow direction, as the cross-sectional area of the channels within the equal pressure ring is smaller, resulting in higher turbulence intensity when the cooling water exits the AG and is distributed to the six pipes within the equal pressure ring, dissipating more energy and leading to greater pressure drop, as well as a more chaotic flow field and poorer flow distribution uniformity. Through analysis, it is concluded that the performance of the channels is acceptable and can meet the cooling water supply requirements.

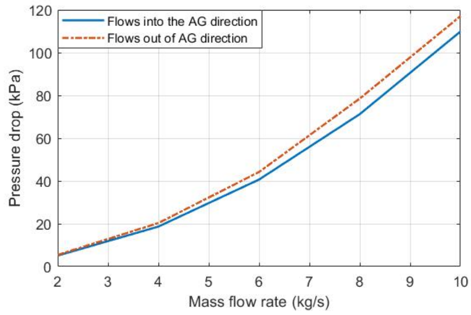

Fig. 8. The relationship between pressure drop and flow rate in the channel.

V. STRUCTURAL STRENGTH

The HV bushing is connected to the SF6 transmission line on one side, subjected to a pressure of $0.6\,\mathrm{MPa}$ of SF6 gas, and connected to an ion source in a vacuum on the other side. Dry air pressure between the ceramic ring and the FRP ring may reach up to $1\,\mathrm{MPa}$. A comprehensive structural strength analysis is conducted considering the gas pressure and the gravitational effects on the bushing. The physical properties of the materials are shown in Tab. 3. The mechanical properties are referenced in Tab. 4, including the tensile strength of the ceramic and Kovar brazed joint as provided by H. Tobari *et al.*, as well as the mechanical properties of two types of FRP materials. The tensile strength at the brazed joint is based on the average value from a specific tensile test, but with a relatively large dispersion.

The Von-Mises stress distribution of the overall structure of the HV bushing is shown in Fig. 10, with the maximum stress point located on the reinforcement rib of the $-400\,\mathrm{kV}$ electrostatic screen cover. The maximum stress of $88.4\,\mathrm{MPa}$ is significantly lower than the tensile strength of stainless steel material. The deformation distribution is shown in Fig. 11, with the maximum deformation of $0.545\,\mathrm{mm}$ occurring at the cover position, which is not significant as it will be connected to the $-400\,\mathrm{kV}$ transmission line. The overall downward deformation of all electrostatic screens is approximately $0.236\,\mathrm{mm}$, mainly caused by the deformation of the $0\,\mathrm{kV}$

TABLE 3. Physical properties of materials.

Material	Elasticity modulus (GPa)	Poisson ratio	Density(kg/m3)
Stainless steel	197	0.29	7930
Kovar	130	0.37	7850
Alumina ceramic	343	0.25	3800
FRP	20	0.3	2200

TABLE 4. Mechanical properties of materials.

Material	Tensile strength (MPa)	Compressive strength(MPa)	Shear strength (MPa)
Filament winding FRP	130	110	25
Fiber cloth FRP	327	279	56
Brazing	103±40	—-	—-
Stainless steel	460	250	—-

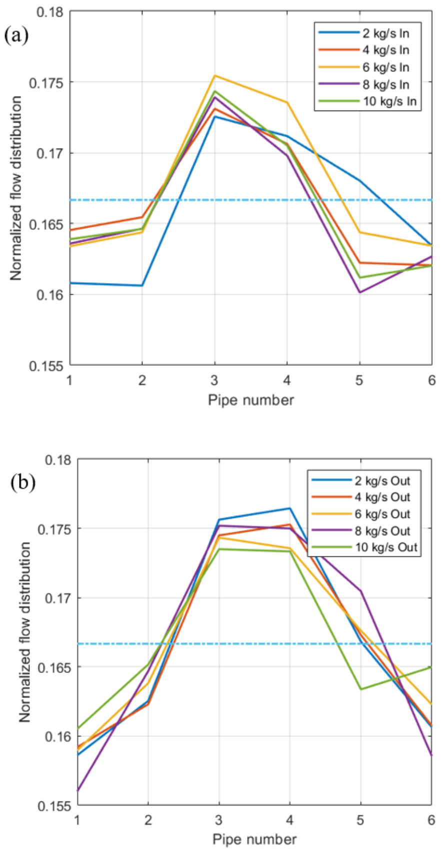

Fig. 9. Flow distribution in parallel pipelines. Cooling water flows into the AG direction (a), Cooling water flows out of AG direction (b).

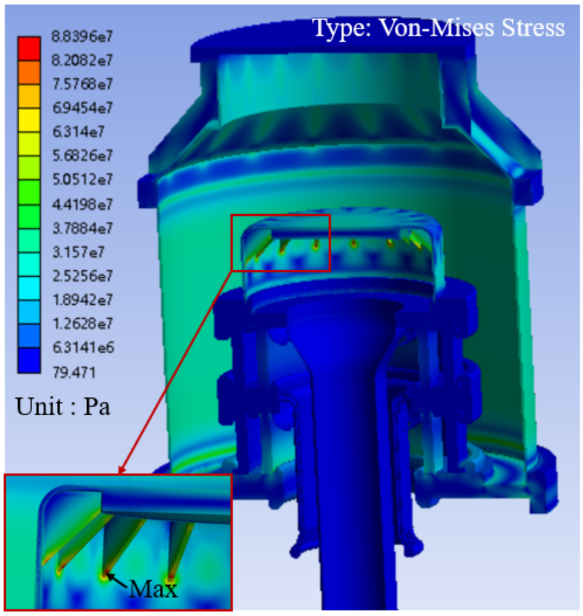

Fig. 10. Von-Mises stress of HV-bushing.

flange under the pressure of SF6 gas, resulting in a relatively small relative deformation of $0.013\,\mathrm{mm}$ between the two electrostatic screens, which cannot be neglected in terms of its impact on the electric field distribution.

The maximum stress near the brazed area on the ceramic ring reaches $24.6\,\mathrm{MPa}$, appearing at the base end of the ceramic ring between $0\,\mathrm{kV}$ and $-200\,\mathrm{kV}$ as shown in Fig. 12. This stress is mainly caused by the deformation of the $0\,\mathrm{kV}$ flange. Designing reinforcement ribs on the $0\,\mathrm{kV}$ flange can reduce the stress on the ceramic ring and the overall structural deformation. The maximum stress on the FRP ring is $6.62\,\mathrm{MPa}$, and the maximum shear stress is $3.81\,\mathrm{MPa}$, also occurring on the FRP ring between $0\,\mathrm{kV}$ and $-200\,\mathrm{kV}$ as shown in Fig. 13. The strength of both manufacturing processes for the FRP meets the requirements.

VI. SUMMARY

The CRAFT NNBI HV bushing is used to connect the SF6 gas transmission line and the vacuum-insulated ion source for the transmission of electrical energy, gas, and cooling water. Preliminary designs were conducted for vacuum insulation, cooling water channels, and structural strength. The results are as follows:

1. The high voltage withstand capability of the vacuum

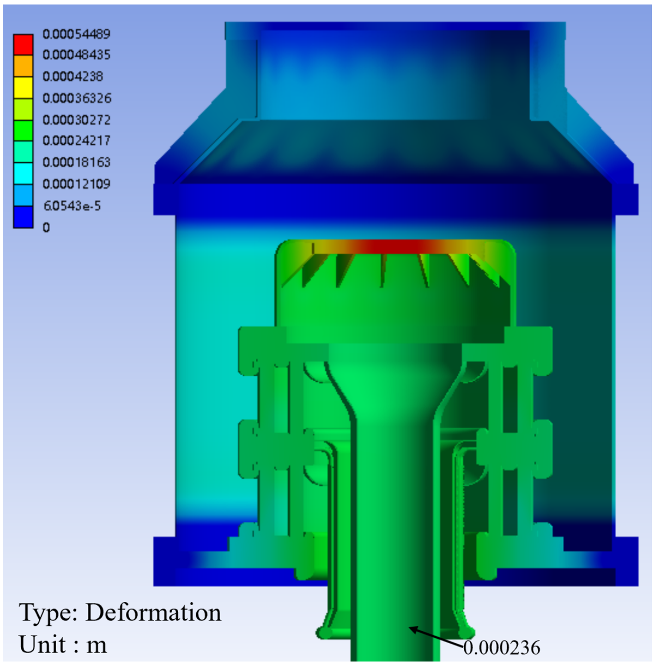

Fig. 11. Deformation of HV-bushing.

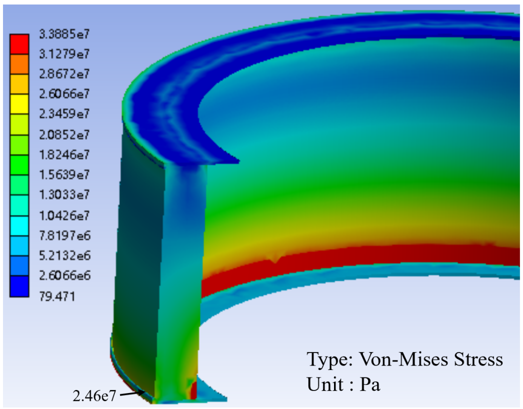

Fig. 12. Von-Mises stress of 0 kV $\sim$ -200 kV ceramic ring.

insulation was calculated using empirical formulas, meeting the voltage requirements. The electric field restriction standards for vacuum insulation were determined, and electric field analysis was performed. The maximum electric field intensity on the cathode surface was $2.93\,\mathrm{kV/mm}$, on the anode surface was $3.69\,\mathrm{kV/mm}$, and on the ceramic insulating ring surface was 0.91 kV/mm, all meeting the standards. The electric field at the vacuum cathode triode point reached $0.17\,\mathrm{kV/mm}$, which did not meet the limiting value. However, based on JAEA's experimental tests, the design of the cathode triode point electric field exceeding the standard limit still meets the insulation requirements.

2. The cooling water channel on the $-200\,\mathrm{kV}$ bushing was designed. Considering the heat load and temperature changes on the AG, the required cooling water flow rate range of 2 to 10 kg/s was determined. A cooling water channel design consisting of six parallel pipes as a group was developed, considering the suppression of unstable flow in parallel channels, with good results. Analysis of pressure drops in the forward and reverse flow of the channels and the flow distribution in parallel pipes was conducted. The maximum pressure drop in the channels did not exceed $120\,\mathrm{kPa}$, within an acceptable range. The flow distribution deviation between parallel pipes was a maximum of 8.3% in the forward direction and 11.5% in the reverse direction.

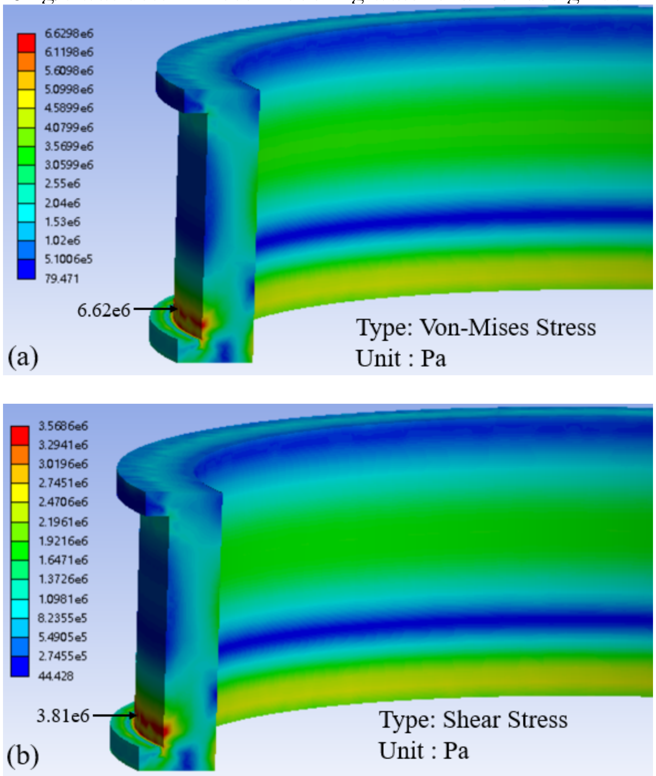

Fig. 13. stress of 0 kV $\sim$ -200 kV FRP ring. Von-Mises stress (a), Shear stress (b).

3. Overall structural strength analysis was conducted, considering the pressure loads of $0.6\,\mathrm{MPa}$ SF6 gas and $1\,\mathrm{MPa}$ air, as well as the self-weight loads. The maximum Von-Mises stress on the stainless steel structure was $88.4\,\mathrm{MPa}$, with the maximum Von-Mises stress near the brazed area of the ceramic insulating ring being $24.6\,\mathrm{MPa}$, and the maximum Von-Mises stress and shear stress on the FRP ring being $6.62\,\mathrm{MPa}$ and $3.81\,\mathrm{MPa}$, respectively. The stresses on each component were significantly lower than the material strength, providing sufficient safety margin. The overall deformation of the bushing was $0.236\,\mathrm{mm}$, with a relative deformation of $0.013\,\mathrm{mm}$ between the electrostatic screens, which would not significantly affect the electric field distribution.

[1] Cui Qinglong, Wei Jianglong, Xie Yahong, et al., Beamlet optics analysis of $400\,\mathrm{keV}$ accelerator for CRAFT negative ion based neutral beam injection system. High Power Laser and Particle Beams **35(11)**, 74-80 (2023). doi: 10.11884/HPLPB202335.230179

[2] HODGSON E R, MORONO A., Radiation effects on insulating gases for the ITER NBI system. J Nucl Mater **258–263**, 1827-1830 (1998). doi: 10.1016/S0022-3115(98)00345-6

[3] Tobari H, Kashiwagi M, Watanabe K, et al., Progress on design and manufacturing of dc ultra-high voltage component for ITER NBI. FUSION Eng Des **123**, 309–312 (2017). doi: 10.1016/j.fusengdes.2017.05.017

[4] Simonin A, de Esch H, Doceul L, et al., Conceptual design of a high-voltage compact bushing for application to future N-NBI systems of fusion reactors. FUSION Eng Des **88(1)**, 1-7 (2013). doi: 10.1016/j.fusengdes.2012.04.025

[5] Tobari H, Taniguchi M, Kashiwagi M, et al., Vacuum Insulation and Achievement of $980\,\mathrm{keV}$, $185\,\mathrm{A/m^2}$ H^- Ion Beam Acceleration at JAEA for the ITER Neutral Beam Injector. Plasma Sci Technol **15(2)**, 179–183 (2013). doi: 10.1088/1009-0630/15/2/21

[6] Wang R, Jiang C, Xu Y, et al., Electrostatic analysis and preliminary design of transmission line for the CRAFT NNBI test platform. FUSION Eng Des **165**, 112259 (2021). doi: 10.1016/j.fusengdes.2021.112259

[7] Xie Y, Hu C, Wei J, et al., Conceptual design of a beam source for negative neutral beam injector of CRAFT facility. Fusion Eng Des **167**, 112377 (2021). doi: 10.1016/j.fusengdes.2021.112377

[8] Tobari H, Watanabe K, Kashiwagi M, et al., DC Ultrahigh Voltage Insulation Technology for 1 MV Power Supply System for Fusion Application. IEEE Trans PLASMA Sci **45(1)**, 162–169 (2017). doi: 10.1103/PhysRevC.87.024603

[9] Cranberg L., The Initiation of Electrical Breakdown in Vacuum. J Appl Phys **23(5)**, 518–522 (1952). doi: 10.1063/1.1702243

[10] Masiello A., Adaptation of the 1 MV bushing to the SINGAP concept for the ITER NB injector test bed. Nucl Fusion **46(6)**, S340–S351 (2006). doi: 10.1088/0029-5515/46/6/S16

[11] Anonymous., ITER Neutral Beam Heating and Current Drive System. Design Description Document. (2001).

[12] Umeda N, Taniguchi M, Kashiwagi M, et al., Development of 1MeV accelerator and HV bushing at JAEA toward ITER Neutral Beam system. Fusion Eng Des **84(7)**, 1875–1880 (2009). doi: 10.1016/j.fusengdes.2008.12.018

[13] Tobari H., Analysis Repoert of HV Bushing for ITER NBTF (Part-1). (2013).

[14] Wei J, Hu C, Xie Y, et al., Physics and engineering design of $400\,\mathrm{keV}$ H^- accelerator for negative ion based neutral beam injection system in China. Rev Sci Instrum **90(11)**, 113313 (2019). doi: 10.1063/1.5128335

[15] Tobari H, Inoue T, Taniguchi M, et al., Structural analyses of HV bushing for ITER heating NB system. Fusion Eng Des **88(6)**, 975–979 (2001). doi: 10.1016/j.fusengdes.2013.02.020